Breaking Wave Simulations of High-speed Surface Combatant using OpenFOAM

Jianhua Wang*, Decheng Wan‡

State Key Laboratory of Ocean Engineering, School of Naval Architecture, Ocean and Civil Engineering, Shanghai Jiao Tong University, Collaborative Innovation Center for Advanced Ship and Deep-Sea Exploration, Shanghai 200240, China

*Presenting author: tjuwjh@126.com

‡Corresponding author: dcwan@sjtu.edu.cn

Abstract

Wave breaking on ship bow, shoulder and stern waves is of great importance for the hydrodynamic performance of high-speed surface ships. In the present work, an unsteady VOF based RANS method is used to resolve and investigate wave breaking around a high-speed surface combatant advancing in calm water. High resolution VOF method with artificial compression technique in OpenFOAM is used to accurately resolve ship bow waves as well as induced free surface scars. In order to provide physical understanding of ship breaking waves, simulations over two ship speeds, i.e. Fr=0.35, Fr=0.41, are carried out. The benchmark ship model DTMB 5415 is used for all the simulations and extensive experimental flow data (provided by INSEAN and IIHR) are available to validate the CFD results. All the computations are carried out by in-house CFD solver naoe-FOAM-SJTU. Predicted ship resistance, wave elevations and flow velocities around ship hull are presented and compared with the experimental measurement. Wave breaking on ship bow waves and stern waves are observed. The induced free surface scars are also resolved and its relation with breaking waves is also analyzed. The CFD solution of ship resistance shows good agreement with the experiment. Comparisons of velocity components at cross planes show that the present VOF based RANS method can accurately predict the wake region associated with breaking wave.

Keywords: Breaking wave, naoe-FOAM-SJTU solver, ship hydrodynamics, DTMB 5415

Introduction

Towing ship in calm water is one of the most fundamental studies in the research of ship hydrodynamics. Despite of the high accuracy of the resistance prediction, it is still challenging to accurately resolve the breaking wave phenomenon, which has long been recognized. Extensive experiments have been performed to try to give the physical understanding of the breaking wave mechanism and CFD validation experimental data. Baba[1] identified a new component of viscous resistance from the experimental study and some theoretical approaches. The author noted that large contribution of resistance is due to the wave breaking of ship bow waves. Duncan[2] conducted measurements for the surface profile and the vertical distributions of velocity of a two-dimensional hydrofoil. The measurements were used to resolve the drag on the foil into two parts: one associate with the turbulent breaking region and the other associate with the remaining non-breaking wavetrain. The measurement showed that the drag associate with breaking reach more than three times the maximum drag that could theoretically be obtained with non-breaking waves. Kayo and Takekuma[3] investigated bow wave breaking phenomenon around full ship models by velocity field measurements and by a flow visualization technique. By use of dye particles placed in front of the bow of full form, the authors find that there exists a shear flow on the free surface. Dong et al.[4] performed experimental study using particle-image-velocimetry (PIV) measurements and free surface visualizations around a ship model at two different speeds, i.e. Fr=0.28 and Fr=0.45. Wave breaking phenomena was observed and the breaking wave associated with vorticity was further discussed. Roth et al.[5] applied the same approach in the experimental study for a 7-meter-long ship model at Froude number of 0.30. Negative vorticity was found at the toe of the wave and positive vorticity appeared on the top of the wave and at the ship boundary. Longo and Stern[6] performed mean velocity measurements using a five-hole Pitot and wave elevation measurements using capacitance wires and point gauges for the static drift condition showing the presence of a bow wave breaking induced vortex on the windward side of the model. Olivieri et al.[7] performed experimental study for the wave breaking of model DTMB 5415, where scars and vortices induced by ship bow and shoulder wave breaking is analyzed. Through measurements of several ship speeds, Fr=0.35 was selected for the intensive study due to the large extents of quasi-steady plunging bow and spilling shoulder wave breaking.

Despite the extensive study through experiment, numerical investigations for the ship breaking waves have also been used as an alternative way to predict and analyze the ship wave breaking phenomena. Wilson et al.[8] applied unsteady single-phase level set RANS method to resolve and investigate bow wave breaking around a surface combatant advancing in calm water, including induced vortices and free surface scars. Good agreement was achieved for both velocity components and axial vorticity at four cross planes and it showed that the CFD approach can accurately predict the detailed flow associate with breaking bow wave. Moraga et al.[9] proposed a sub-grid air entrainment model for breaking bow waves and applied for the simulation of naval surface ship DTMB 5415 and Athena. The model compared favorably with data at laboratory scale and also presented the right trends at full-scale. Marrone et al.[10,11] studied ship wave breaking patterns using both 2D+t and 3D meshless SPH simulations. Through comparison with the experimental data, the proposed schemes were proved to be robust and accurate in simulating ship wave breaking. Landrini et al.[12] presented splashing bow wave simulations using a hybrid BEM-SPH method. A domain-decomposition strategy was adopted which combines two Lagrangian methods, where a potential-flow solution, given by a boundary element method (BEM), follows the jet evolution up to the breaking and then initiates a rotational solution, provided by a smoothed particle hydrodynamics (SPH) technique. Noblesse et al.[13] reviewed the recent results about the overturning and breaking bow wave regimes, and the boundary that divides these two basic flow regimes. Questions and conjectures about the energy of breaking ship bow waves, and free-surface effects on flow circulation, are also noted.

Previous numerical studies on the ship wave breaking are mostly based on the level set approach or the meshless Lagrangian method. In the present work, high resolution Volume of Fluid (VOF) method is used to accurately resolve the large deformation of free surface. The main framework of this paper goes as following. The first part is the numerical methods, where VOF method and numerical schemes are presented. The second part is the geometry model and test conditions. Then comes the simulation part, where wave breaking simulations are present at different Froude numbers. In this part, extensively comparisons are performed against the experimental measurements including ship resistance, wave patterns and wake profiles at longitudinal slices. Finally, a conclusion of this paper is drawn.

Numerical methods

Governing equations

The in-house CFD solver naoe-FOAM-SJTU[14–16], developed on open source platform OpenFOAM, applied in this study solves the Reynolds-Averaged Navier-Stokes equations for unsteady turbulent flows and VOF method is used to capture free surface around the complex geometry models. The URANS equations are written as a mass conservation equation and a momentum conservation equation:

$$\nabla \cdot \boldsymbol{U} = 0 \tag{1}$$

$$\frac{\partial \rho \boldsymbol{U}}{\partial t} + \nabla \cdot \left[(\rho \boldsymbol{U} - \boldsymbol{U}_g)\boldsymbol{U} \right] = -\nabla p_{\mathrm{d}} - \boldsymbol{g} \cdot \boldsymbol{x} \nabla \rho + \nabla \cdot (\mu_{eff} \nabla \boldsymbol{U}) + (\nabla \boldsymbol{U}) \cdot \nabla \mu_{eff} + f_\sigma \tag{2}$$

where $\boldsymbol{U}$ is the fluid velocity field and $\boldsymbol{U_g}$ is the velocity of mesh points; $p_d = p - \rho \boldsymbol{g} \cdot \boldsymbol{x}$ is the dynamic pressure, obtained by subtracting the hydrostatic component from the total pressure; ρ is the mixture density of the two-phase fluid; $\boldsymbol{g}$ is the gravity acceleration; $\mu_{\mathrm{eff}} = \rho(\nu + \nu_t)$ is the effective dynamic viscosity, in which ν and ν_t are the kinematic viscosity and kinematic eddy viscosity respectively, the latter one is obtained by the two-equation shear stress transport turbulence model $SST\ k-\omega$[17]; f_σ is a source term due to surface tension.

VOF method and surface tension

For the wave breaking simulations, the free surface capture method plays an important role in the accuracy of predicted results. In the present work, VOF method with bounded compression technique[18] is applied to capture free surface and the transport equation is expressed as:

$$\frac{\partial \alpha}{\partial t} + \nabla \cdot \left[\left(\boldsymbol{U} - \boldsymbol{U}_{\mathrm{g}} \right) \alpha \right] + \nabla \cdot \left[\boldsymbol{U_r} \left(1 - \alpha \right) \alpha \right] = 0 \tag{3}$$

where α is volume of fraction, 0 and 1 represent that the cell is filled with air and water respectively and $0 < \alpha < 1$ stands for the interface between two-phase fluid. $\boldsymbol{U_r}$ in Eqn. (3) is the velocity field used to compress the interface and it only takes effect on the free surface due to the term $(1-\alpha)\alpha$.

According to the literature concerning wave breaking, small scale wave breaking is strongly influenced by surface tension. The role played by the surface tension is quite different for breaking and non-breaking waves since the surface tension pressure jump depends on the magnitude of the radius of curvature of the free surface. In order to reappear the wave patterns of the experiment, the surface tension is taken account in the present simulation and the surface tension term mentioned in Eqn. (2) is expressed as:

$$f_\sigma = \sigma \kappa \nabla \alpha \tag{4}$$

where σ stands for the surface tension, κ is the curvature of free surface and it is defined as:

$$\kappa = -\nabla \cdot \boldsymbol{n} = -\frac{\sum_f \boldsymbol{S}_f \cdot \boldsymbol{n}_f}{V_i} \tag{5}$$

V_i represents the volume of cell i, $\sum_f \boldsymbol{S}_f$ stands for the sum of value on each face of cell.

Finite volume method (FVM) with fully unstructured grids is used to transform the RANS and VOF equations from physical space into computational space. The merged PISO-SIMPLE (PIMPLE) algorithm is applied to solve the coupled equations for velocity and pressure field. The Semi-Implicit Method for Pressure-Linked Equations (SIMPLE) algorithm allows to couple the Navier-Stokes equations with an iterative procedure. And the Pressure Implicit Splitting Operator (PISO) algorithm enables the PIMPLE algorithm to do the pressure-velocity correction. Detailed description for the SIMPLE and PISO algorithm can be found in Ferziger and Peric[19] and Issa[20]. Near wall treatment wall functions are applied to the moving wall boundary. In addition, several built-in numerical schemes in OpenFOAM are used in discretizing and solving the partial differential equations (PDE). The convection terms are discretized by a second-order TVD limited linear scheme, and the viscous terms are approximated by a second-order central difference scheme. A second-order backward scheme is used for temporal discretization except the VOF advection equation, where Euler scheme is adopted.

Geometry model and test conditions

Geometry model

The geometry model of interest is the surface combatant model DTMB 5415 and the numerical simulations are conducted using 5.72 m replica (INSEAN Model 2340). The geometry model of the ship model is shown in Fig. 1, and its principle parameters are listed in Table 1. Extensive experiments have been conducted for the ship model under various Froude numbers and photo study is also available through the experimental measurements[7]. The available experimental data, i.e. ship resistance, wave patterns and flow velocities around ship hull, can be used to validate our present computational results.

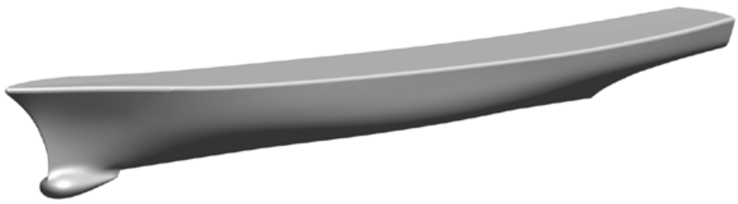

Fig. 1 Geometry model of DTMB 5415 (INSEAN Model 2340)

Table 1 Principle dimensions of DTMB 5415

Main particulars		Model scale	Full scale
Scale factor	λ	24.824	1
Length between perpendiculars	$L_{pp}(m)$	5.719	142.0
Maximum beam of waterline	$B_{WL}(m)$	0.768	19.06
Draft	$T\ (m)$	0.248	6.15
Displacement volume	$\Delta\ (m^3)$	0.554	84244
Wetted surface area	$S_0\ (m^2)$	4.786	2972.6
Metacentric height	$GM\ (m)$	NA	1.95
Moment of inertia	K_{xx}/B_{WL}	NA	0.37
	K_{yy}/L_{WL}, K_{zz}/L_{WL}	0.252	0.25

According to the literature concerning wave breaking, the phenomena are strongly connected with turbulence generation, which, in other words, is a viscous phenomenon. Hence, the turbulence parameters should be considered carefully in the numerical simulations. Table 2 summarizes the water quality and physical quantities adopted in the experiments and simulations.

Table 2 Physical quantities in experiment and simulation

Parameters	Symbol	Experiment	Simulation	Full scale
Water density	$\rho\ (kg/m^3)$	998.5*	998.5	1030*
Kinematic viscosity	$\nu\ (m^2/s)$	1.09×10^{-6}	1.09×10^{-6}	1.17×10^{-6}
Surface tension	$\sigma\ (N/m)$	0.0734	0.0734	0.0734
Gravity acceleration	$g\ (m/s^2)$	9.8033*	9.81	9.806*

*Data taken from literature.

Test conditions

The present work is for the wave breaking simulation DTMB 5415 bare hull model. Two approaching speeds corresponding to Froude number of $Fr = 0.35$ and $Fr = 0.41$, are taken into account to investigate the wave breaking behavior. During the simulations, the model was held fixed with sinkage and trim set to the values previously determined in unrestrained conditions[21]. The simulation conditions are tabulated in Table 3.

Table 3 Simulation conditions for DTMB 5415

Froude number	Speeds (m/s)	Trim(deg)	Sinkage(Lpp)
0.35	2.621	0.069	0.0032
0.41	3.071	-0.421	0.0047

Computational overview

Fully unstructured grids used in this paper are generated by *snappyHexMesh* with the background grid generated by *blockMesh*, both are pre-processing utilities provided by OpenFOAM. In order to accurately capture the breaking wave phenomenon, several refinement regions have been adopted and the grid distribution is shown in Fig. 2. As the ship model is fixed with corresponding trim and sinkage, only half of the flow domain is modeled. The total grid number in the present simulation is 18.7 million.

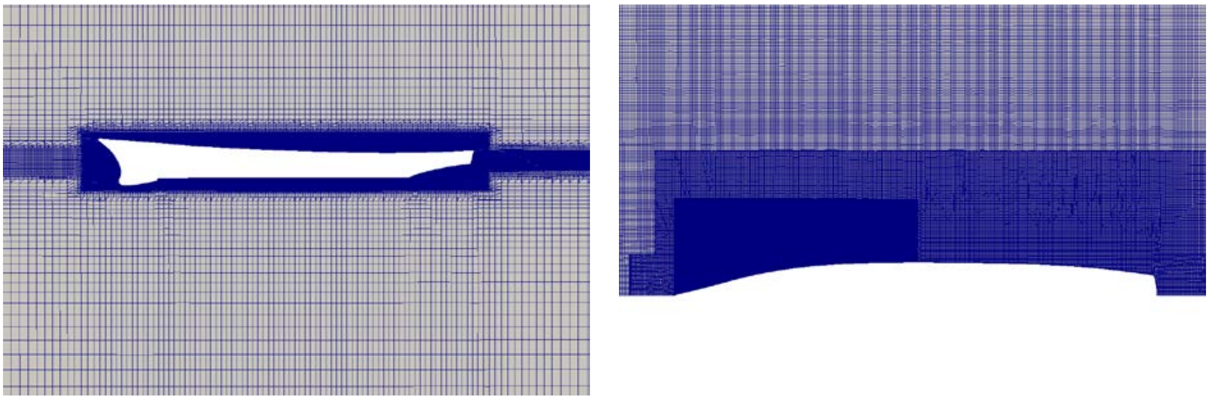

a) Profile of grid distribution b) Grid arrangement at free surface

Fig. 2 Grid distribution around ship hull

Simulation results and analysis

The computations are carried out on a HPC cluster (IBM nx360M4) in Shanghai Jiao Tong University, which consist of 20 CPUs per node and 64GB accessible memory (Intel Xeon E5-2680v2 @2.8 GHz). 128 processors are assigned to calculate the wave breaking cases under different ship speeds. The time step was set to $\Delta t = 0.001s$, and time to complete the computation was approximately 136 wall clock hours and 17369 CPU hours with about 35000 time steps for the wave breaking simulation.

Fr=0.35

As mentioned in Table 3, the simulation case for Fr=0.35 is under ship speeds of $U = 2.621 m/s$ and the ship model is fixed with the initial sinkage of 0.0032Lpp and trim of 0.069deg. Two grids are adopted in the simulation of Fr=0.35 case, one has 18.7 million cells as shown in Fig. 2b and another one has 12 million cells with no refinement in the bow region. Fig. 3 shows the wave pattern with different grids. Significant difference can be observed for the bow waves surrounded by the red box, which indicates that the density of the grid in the bow wave region can strongly affect the bow wave breaking phenomena.

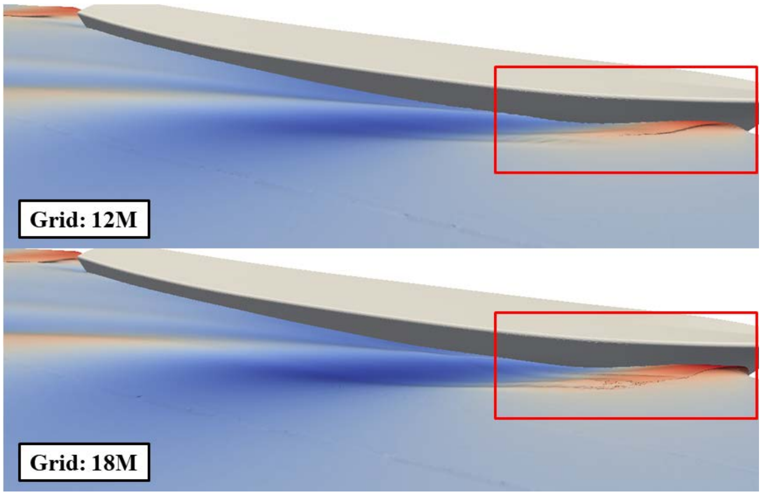

Fig. 3 Wave pattern with different grids

Table 4 Total resistance comparison at Fr=0.35

Cases	Grid number (Million)	Total resistance (N)	Error (%)
Fine grid	18.7	78.33	-2.86
Coarse grid	12.4	78.15	-3.09
Experiment[21]	--	80.64	--

Despite the different wave pattern with fine and coarse grids, the predicted ship resistance agrees very well with the experiment, which indicates that the grid density has little influence on the resistance when grid number is over 10 million for RANS computation. The finer mesh can give promising result of the bow wave pattern according to the experimental measurements, where two scars can be formed due to the evolution of the bow wave. As shown in Fig. 4a, the bow wave breaking phenomena can be obviously observed, and furthermore, the stern wave breaking can also be captured shown in Fig. 4b.

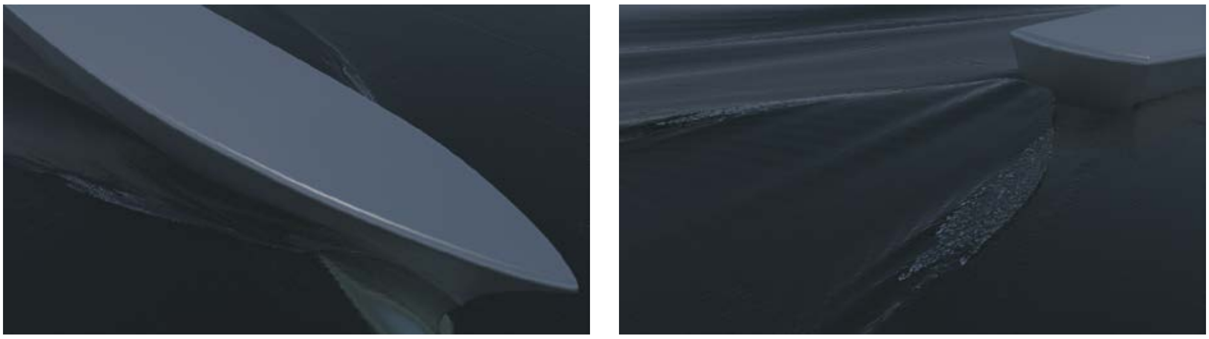

a) Bow wave breaking b) Stern wave breaking

Fig. 4 Simulation results of bow and stern wave breaking at Fr=0.35

The simulation for present Fr=0.35 case and Fr=0.41 talked in the next section adopt the finer grids with about 18.7 million cells. In order to validate the present CFD results, detailed flow velocities at two cross sections are presented and compared with the available experimental measurements[7]. The two cross sections ($x/L_{pp}=0.15$, $x/L_{pp}=0.40$) correspond to the bow and shoulder waves and flow patterns, respectively. Fig. 5 and Fig. 6 illustrate the nondimensionalized mean velocity components (i.e. $(u,v,w)=(U_x,U_y,U_z)/U$) at $x/L_{pp}=0.15$ and $x/L_{pp}=0.40$, respectively. Left figures are the CFD simulation results and right column are the experimental measurements.

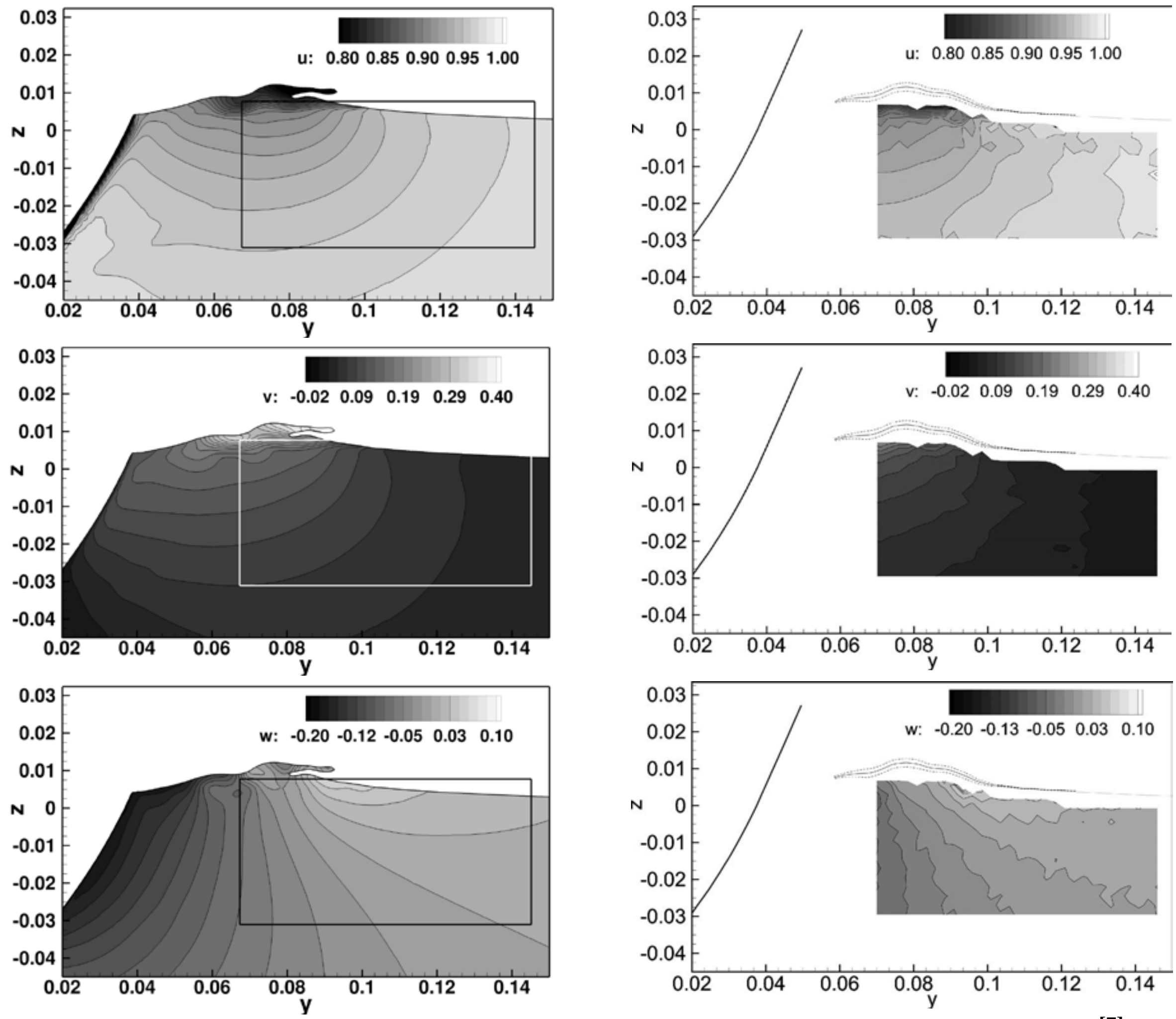

Fig. 5 Velocity components at $x/L_{pp}=0.15$ (left: CFD results, right: experiment[7])

The rectangle box on the CFD figures stands for the area measured experimentally. The agreement between CFD and EFD is satisfactory in both sections for the three-velocity components. It can be obviously seen that at section $x/L_{pp}=0.15$, the bow wave shows a plunging type breaker, while at section $x/L_{pp}=0.40$, the shoulder wave appears as spilling type breaker. The same phenomena have also been observed from the experiment measurement. Apart from the bow wave and shoulder wave that were measured in the experiments, the stern wave breaking shown in Fig. 4b can also be resolved. The wave breaking is formed as plunging type, which is the same with the bow wave breaking. Furthermore, the stern wave breaking can be extended to a larger area according to the present simulation.

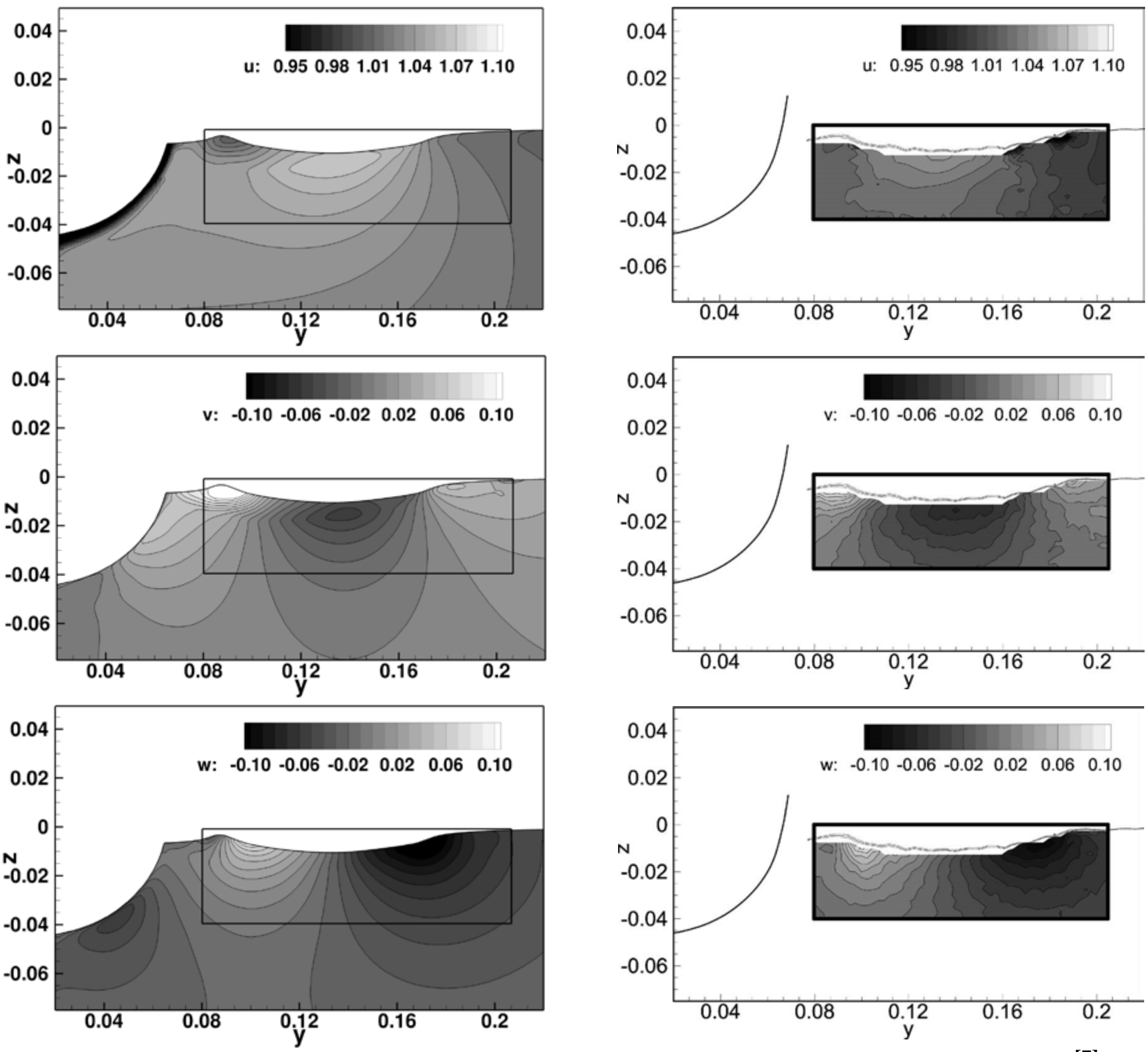

Fig. 6 Velocity components at $x/L_{pp}=0.40$ (left: CFD results, right: experiment[7])

Scars in bow wave breaking of the experiments and present CFD results are shown in Fig. 7. It can be clearly seen with the overturning bow wave and the formation of the scars in the CFD slices of free surface at bow region. Dashed lines show the predicted scars in the bow wave and agree well with the measurements, which show that the URANS approach with VOF method can be robust and reliable in predicting the bow wave breaking of high speed naval ships.

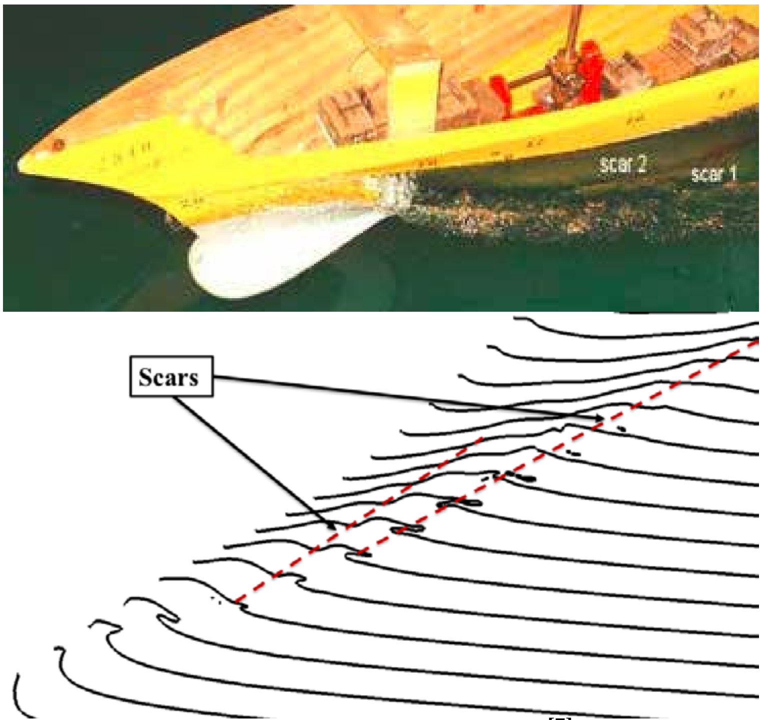

Fig. 7 Scars in bow wave breaking (top: experiment[7], bottom: present result)

Fr=0.41

The higher ship speed with Froude number of 0.41 has also been simulated with the same grids and numerical setup of the Fr=0.35 case. Since there is no available experimental flow data, only total resistance is compared with the measurement. Present CFD prediction of total resistance is just over-estimated by 1.59% compared with the towing tank result[21], which confirms that the CFD simulation is reliable.

Table 5 Total resistance comparison at Fr=0.41

Cases	Grid number (Million)	Total resistance (N)	Error (%)
CFD	18.7	155.02	1.59
Experiment[21]	--	152.59	--

Three velocity components at two cross sections ($x/L_{pp}=0.15$, $x/L_{pp}=0.40$) are shown in Fig. 8. Left column shows the bow wave breaking region and right column is the shoulder wave breaking region. At section $x/L_{pp}=0.15$, the free surface shows more unsteady than that of Fr=0.35. This phenomenon is mainly caused by the ship speeds, where the bow wave formed earlier and the wave height is much larger. The bow wave breaking of ship model appears in the form of a plunging breaker with evidence of the overturning of the wave crest. Air entrainment is considerably increased in this case. At section $x/L_{pp}=0.40$, the shoulder wave also differs a lot with that of Fr=0.35 case, where the shoulder wave is merging with the hull. Furthermore, the bow wave can also be found and it forms a spilling type wave breaker as shown in the shoulder wave section.

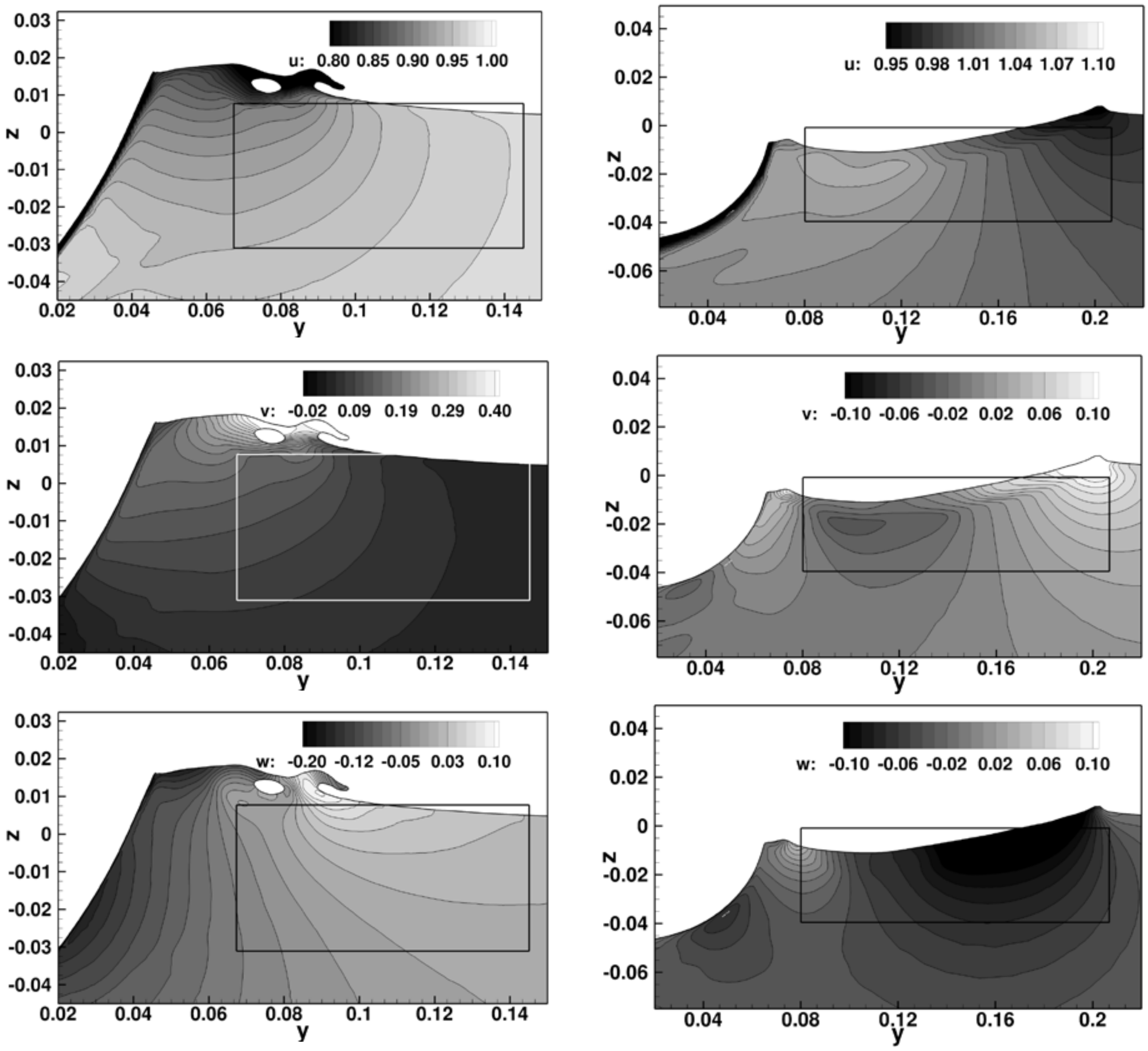

Fig. 8 Velocity components (left: $x / L_{pp} = 0.15$, right: $x / L_{pp} = 0.40$)

Bow wave evolution can be better recognized in Fig. 9a and Fig. 10. The unsteady plunging breaker extends to a larger area compared with Fig. 4a and the scars is also more obvious. Fig. 9b shows the stern wave at Fr=0.41 and from the figure we can see that the wave pattern differs a lot with Fig. 4b. A steady state is presented and the stern wave crest is higher than that at Fr=0.35.

a) Bow wave breaking

b) Stern wave breaking

Fig. 9 Simulation results of bow and stern wave breaking at Fr=0.41

Scars at bow wave breaking are illustrated in Fig. 10. There are two obvious overturning of the bow wave, thus result in severe air entrainment. Different from the Fr=0.35 case, the overturning bow wave appears earlier and the air entrainment extends to a larger range in longitudinal direction.

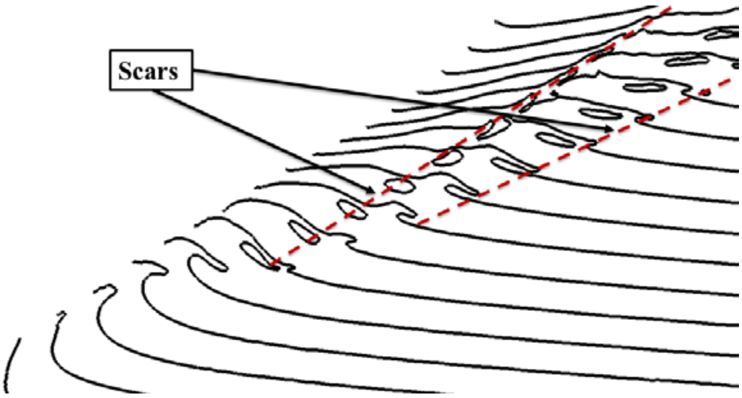

Fig. 10 Scars in bow wave breaking at Fr=0.41

Conclusions

This paper presents the breaking wave simulations of surface combatant DTMB model 5415 at two different speeds, i.e. Fr=0.35, Fr=0.41. All the simulations are performed using in-house CFD solver naoe-FOAM-SJTU. During the simulation, high resolution VOF method with artificial compression technique in OpenFOAM is used to accurately resolve ship bow waves as well as induced free surface scars.

Predicted ship resistance agrees very well with the towing tank measurement. Two grids are adopted for the simulation of wave breaking at Fr=0.35. Both grids give promising results of ship resistance, while the finer grid can better resolve the bow breaking phenomenon. Three velocity components at two cross sections, $x/L_{pp}=0.15$ and $x/L_{pp}=0.40$ corresponding to the bow wave and shoulder wave region, are compared with the available experiment measurements. Good agreement is achieved and bow wave evolution has also been presented and compared with the photo taken using high speed cameras. Plunging breaker for the bow wave and spilling type for the shoulder wave is captured by both CFD and experiment measurement. Furthermore, the CFD simulation also gives the stern wave at Fr=0.35, which shows unsteady plunging type wave breaking. Fr=0.41 shows much difference for the wave patterns with the Fr=0.35 case. Air entrainment can be obviously observed and the bow wave breaking is more unsteady. Shoulder wave is merging to the hull and the bow wave can affect a larger area in the longitudinal direction. Two overturning waves can be captured and thus result in the severe air entrainment.

Future work will focus on the detailed analysis with the vortices associate with the breaking waves. More work will be done to do the wave breaking simulations for the container ship KCS under high speeds, which will be presented at the 2020 CFD workshop in ship hydrodynamics.

Acknowledgements

This work is supported by the National Natural Science Foundation of China (51379125, 51490675, 11432009, 51579145), Chang Jiang Scholars Program (T2014099), Shanghai

Excellent Academic Leaders Program (17XD1402300), Program for Professor of Special Appointment (Eastern Scholar) at Shanghai Institutions of Higher Learning (2013022), Innovative Special Project of Numerical Tank of Ministry of Industry and Information Technology of China (2016-23/09) and Lloyd's Register Foundation for doctoral student, to which the authors are most grateful.

References

[1] Baba, E. (1969) A New Component of Viscous Resistance of Ships, *Journal of the Society of Naval Architects of Japan* **125**, 23–34.

[2] Duncan, J.H. (1983) The breaking and non-breaking wave resistance of a two-dimensional hydrofoil, *Journal of Fluid Mechanics* **126**, 507–520.

[3] Kayo, Y., and Takekuma, K. (1981) On the Free-Surface Shear Flow related to Bow Wave-Breaking of Full Ship Models, *Journal of the Society of Naval Architects of Japan* **149**, 11–20.

[4] Dong, R.R., Katz, J., and Huang, T.T. (1997) On the structure of bow waves on a ship model, *Journal of Fluid Mechanics* **346**, 77–115.

[5] Roth, G.I., Mascenik, D.T., and Katz, J. (1999) Measurements of the flow structure and turbulence within a ship bow wave, *Physics of Fluids* **11**(11), 3512–3523.

[6] Longo, J., and Stern, F. (2002) Effects of drift angle on model ship flow, *Experiments in Fluids* **32**(5), 558–569.

[7] Olivieri, A., Pistani, F., Wilson, R., Campana, E.F., and Stern, F. (2007) Scars and Vortices Induced by Ship Bow and Shoulder Wave Breaking, *Journal of Fluids Engineering* **129**(11), 1445–1459.

[8] Wilson, R.V., Carrica, P.M., and Stern, F. (2006) URANS simulations for a high-speed transom stern ship with breaking waves, *International Journal of Computational Fluid Dynamics* **20**(2), 105–125.

[9] Moraga, F.J., Carrica, P.M., Drew, D.A., and Lahey, R.T. (2008) A sub-grid air entrainment model for breaking bow waves and naval surface ships, *Computers & Fluids* **37**(3), 281–298.

[10] Marrone, S., Colagrossi, A., Antuono, M., Lugni, C., and Tulin, M.P. (2011) A 2D+t SPH model to study the breaking wave pattern generated by fast ships, *Journal of Fluids and Structures* **27**(8), 1199–1215.

[11] Marrone, S., Bouscasse, B., Colagrossi, A., and Antuono, M. (2012) Study of ship wave breaking patterns using 3D parallel SPH simulations, *Computers & Fluids* **69**, 54–66.

[12] Landrini, M., Colagrossi, A., Greco, M., and Tulin, M.P. (2012) The fluid mechanics of splashing bow waves on ships: A hybrid BEM–SPH analysis, *Ocean Engineering* **53**, 111–127.

[13] Noblesse, F., Delhommeau, G., Liu, H., Wan, D., and Yang, C. (2013) Ship bow waves, *Journal of Hydrodynamics, Ser B* **25**(4), 491–501.

[14] Shen, Z., Cao, H., Ye, H., and Wan, D. (2012) The manual of CFD solver for ship and ocean engineering flows: naoe-FOAM-SJTU, Shanghai Jiao Tong University.

[15] Cao, H., and Wan, D. (2014) Development of Multidirectional Nonlinear Numerical Wave Tank by naoe-FOAM-SJTU Solver, *International Journal of Ocean System Engineering* **4**(1), 52–59.

[16] Shen, Z., Wan, D., and Carrica, P.M. (2015) Dynamic overset grids in OpenFOAM with application to KCS self-propulsion and maneuvering, *Ocean Engineering* **108**, 287–306.

[17] Menter, F.R., Kuntz, M., and Langtry, R. (2003) Ten years of industrial experience with the SST turbulence model, *Turbulence, Heat and Mass Transfer* **4**(1), 625–632.

[18] Weller, H.G. (2008) A new approach to VOF-based interface capturing methods for incompressible and compressible flow, OpenCFD Ltd, Report TR/HGW/04.

[19] Ferziger, J.H., and Peric, M. (2012) Computational methods for fluid dynamics, Springer Science & Business Media.

[20] Issa, R.I. (1986) Solution of the implicitly discretised fluid flow equations by operator-splitting, *Journal of Computational Physics* **62**(1), 40–65.

[21] Olivieri, A., Pistani, F., Avanzini, A., Stern, F., and Penna, R. (2001) Towing tank experiments of resistance, sinkage and trim, boundary layer, wake, and free surface flow around a naval combatant INSEAN 2340 model, IIHR Report No 421.